Supporting Information for Design of multimodal absorption in the mid-IR: a metal dielectric metal approach

Nelson W. Pech-May,[*,†,‡] Tobias Lauster,[†,¶] and Markus Retsch[*,†,¶]

†*Department of Chemistry, Physical Chemistry I, University of Bayreuth, Universitätsstr. 30, 95447 Bayreuth, Germany*
‡*Bundesanstalt für Materialforschung und -prüfung (BAM), 12200 Berlin, Germany*
¶*Bavarian Polymer Institute, University of Bayreuth, Universitätsstr. 30, 95447 Bayreuth, Germany*

E-mail: nelson.pech@uni-bayreuth.de; markus.retsch@uni-bayreuth.de

Contents

1 DESCRIPTION OF MAGNETIC POLARITON RESONANCES

1.1 COMSOL simulations

We have built a 3D geometry for performing simulations with COMSOL®Multiphysics using the Wave Optics Module.[1] Figure 1a shows an isometric view of the modeling setup. In the center, there is a Au-ZnS-Au unit cell on a Si substrate. Above this, there is an air layer. This whole geometry is enclosed by two Perfectly Matched Layers (PMLs), one above the air layer and another one below the Si substrate. PMLs allow our truncated domain to be a reasonable approximation of free space. A truncated domain is wanted to keep the size of the model as small as possible and to reduce computational costs. Moreover, PMLs are domains added along the exterior of a model that should absorb all outgoing waves. However, in practice a very small reflection is obtained ($\sim 10^{-7}$) for incidence angles from 0°- 60°. This is due to the finite size of the mesh.

Additionally, we need to model a 2D periodic array of Au discs on top of a ZnS-Au-Si substrate (see Figure 1 of the main text). Therefore, we impose periodic boundary conditions

on the four lateral sides of the 3D geometry presented in Figure 1a. The Bloch-Floquet theorem gives a powerful mathematical simplification for the electromagnetic waves evolving in a periodic potential or lattice: the solutions of the characteristic Maxwell equation in this case are not pure plane waves (as in free space), but can be described as plane waves which are modulated by a function having the periodicity of the lattice.[2] This saves a huge amount of computational costs.

A lateral view of the zoomed central region of the 3D geometry is shown in Figure 1b. The Au elements (100 nm thickness) are highlighted in blue color. The ZnS layer (200 nm thickness) is separating the Au film and the Au disc, as indicated by an arrow. The regions which are not marked by arrows correspond to air or Si.
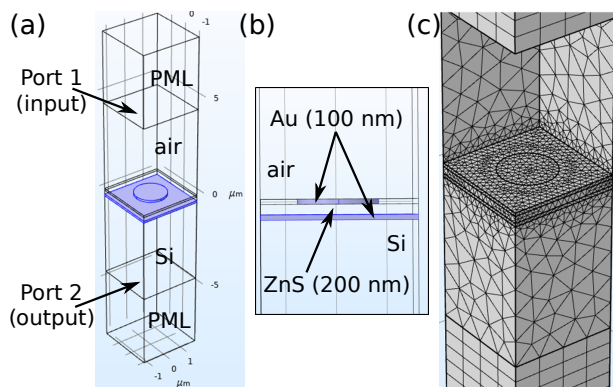

Figure 1: (a) Geometry interface used for the COMSOL simulations. (b) Zoom in of the MDM structure in the geometry setup. (c) Exemplary mesh generated before the computation of the solution by the finite element method.

Figure 1c shows a zoomed image of an exemplary mesh construction. This mesh is used for computing the results using the finite element method. The mesh is optimized such that it is finer for the smallest structures and gradually increases on the larger elements of the geometry. This contributes to reduce the simulation time significantly. In this view, some sections of the air layer are hidden for visualization purposes only. However, the whole geometry is meshed for the calculations.

The electromagnetic waves, frequency domain (ewfd) interface was used for computing the re-

flectance (R) and transmittance (T) spectra in all simulations performed in this work. Ports 1 and 2, shown in Figure 1a, are used to compute $R = |S_{11}|^2$ and $T = |S_{21}|^2$, respectively. The S-parameters are defined as:[3]

$$S_{11} = \frac{\int_{\partial\Omega} \left(\vec{\mathbf{E}}_c - \vec{\mathbf{E}}_1\right) \cdot \vec{\mathbf{E}}_1^*}{\int_{\partial\Omega} |\vec{\mathbf{E}}_1|^2}, \qquad (1)$$
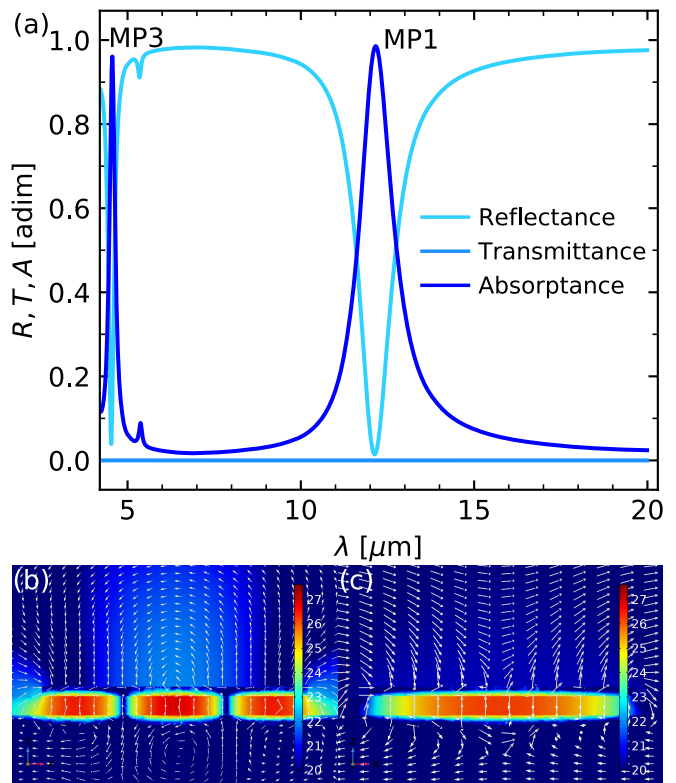

Figure 2: (a) Transmittance (T), reflectance (R) and absorptance (A) spectra for a Au-ZnS-Au periodic array on Si with discs of 2.8 μm diameter. Magnetic field ($\log|H_y|^2$) localization in the cross-section of a unit cell and distribution of the electric displacement field (white arrows) for: (b) the third-mode (MP3) of the magnetic polariton and (c) the first-mode (MP1) of the magnetic polariton.

$$S_{21} = \frac{\int_{\partial\Omega} \left(\vec{\mathbf{E}}_c - \vec{\mathbf{E}}_2\right) \cdot \vec{\mathbf{E}}_2^*}{\int_{\partial\Omega} |\vec{\mathbf{E}}_2|^2}, \qquad (2)$$

where $\vec{\mathbf{E}}_c$ is the total computed electric field at the corresponding port boundary. The electric fields $\vec{\mathbf{E}}_1$ and $\vec{\mathbf{E}}_2$ are fundamental modes obtained by an eigenmode expansion of the elec-

tromagnetic fields at ports 1 and 2, respectively. The integrals are evaluated over the surface $\partial\Omega$ of the corresponding port and $(\cdot)^*$ is the complex conjugate operator. All the absorptance spectra were obtained using $A = 1 - R - T$.

Figure 2a shows the transmittance, reflectance and absorptance spectra computed for a periodic square array of Au discs of 100 nm thickness and 2.8 μm diameter on a ZnS-Au-Si substrate. The period of the 2D array is $\Lambda = 4$ μm. Two main resonances are observed at $\lambda_{MP3} = 4.53$ μm and $\lambda_{MP1} = 12.13$ μm, which are attributed to the third and first modes of the magnetic polariton (MP), respectively. To show that these resonances do not correspond to surface plasmon polariton (SPP) excitations due to a 2D grating coupling, we have calculated the SPP resonances (λ_{SPP}) for a 2D periodic array of Au discs on a Au substrate using the implicit relation:[4]

$$\lambda_{SPP} = \frac{\Lambda}{\sqrt{j^2 + k^2}} \Re\left(\frac{\epsilon_m(\lambda)\epsilon_d}{\epsilon_m(\lambda) + \epsilon_d}\right), \quad (3)$$

where $\Lambda = 4$ μm is the period of the 2D grating, $(j, k) = \{(\pm 1, 0), (\pm 1, \pm 1), (\pm 2, 0), ...\}$ is the mode order index for the corresponding SPP resonance and $\Re(\cdot)$ stands for the real part operator. The complex dielectric function of Au $\epsilon_m(\lambda)$ is taken from literature and ϵ_d is the dielectric function of air. We have found that $\lambda_{SPP} \sim 4$ μm for the mode order $(\pm 1, 0)$ and shift to shorter wavelengths for higher diffraction orders. Consequently, the modes obtained in this work cannot be due to SPP excitations and are identified as MP resonances . However, it is possible to couple a SPP resonance (for a given fixed period) to a MP resonance by adjusting the diameter of the disc. The SPP-MP mode coupling is out of the scope of this work.

Cross-sections of the magnetic field localization for these resonant modes are shown in Figure 2b and Figure 2c, for MP3 and MP1, respectively. In the case of MP1, the magnetic field is completely localized in the ZnS layer, between the Au thin film and the Au disc. On the other hand, for MP3, the localization of the magnetic field is three-folded in the same region. Additionally, arrows represent the electric
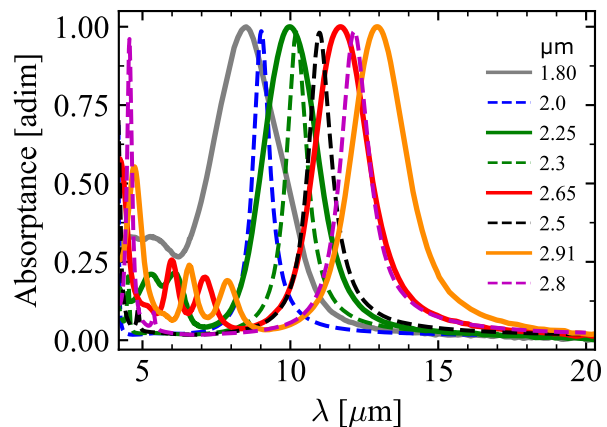

Figure 3: Comparison between absorptance spectra computed with COMSOL (dashed lines) and the measured spectra from the fabricated samples (continuous lines). The diameters of the Au discs are given in μm.

displacement field distribution.

Additionally, we present a comparison between the absorptance spectra computed with COMSOL and the measured spectra from the fabricated samples. Figure 3 shows the comparison of the spectra computed with COMSOL (Figure 1b of the main text) and the corresponding measured spectra (Figure 3a of main text) for Au disc diameters of similar size. Note that experimentally the diameters of the Au discs slightly differ from the simulated ones, therefore, the measured spectra are different from the simulated ones. Nevertheless, the correspondence between the simulations and experimental results is clear. The measured spectra are normalized with respect to the maximum peak absorptance for easier comparison of the peak wavelengths. As can be seen in Figure 3a of the main text, the maximum absorptance obtained is for all cases less than one. This can be attributed to differences in the complex dielectric function of the materials used with respect to the literature values used in the simulations. A note regarding the full-width at half-maximum is given below (see section Full-Width at Half-Maximum (FWHM)).

1.2 LC model

Figure 4 shows a diagram of the equivalent inductor-capacitor circuit (LC model) used to
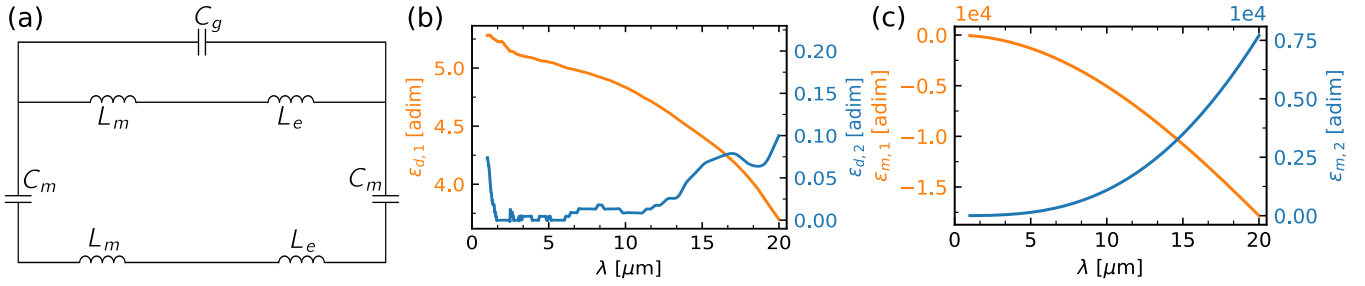
Figure 4: (a) Diagram of the LC-circuit used to model the magnetic polariton resonances. Dielectric function of (b) ZnS and (c) Au.
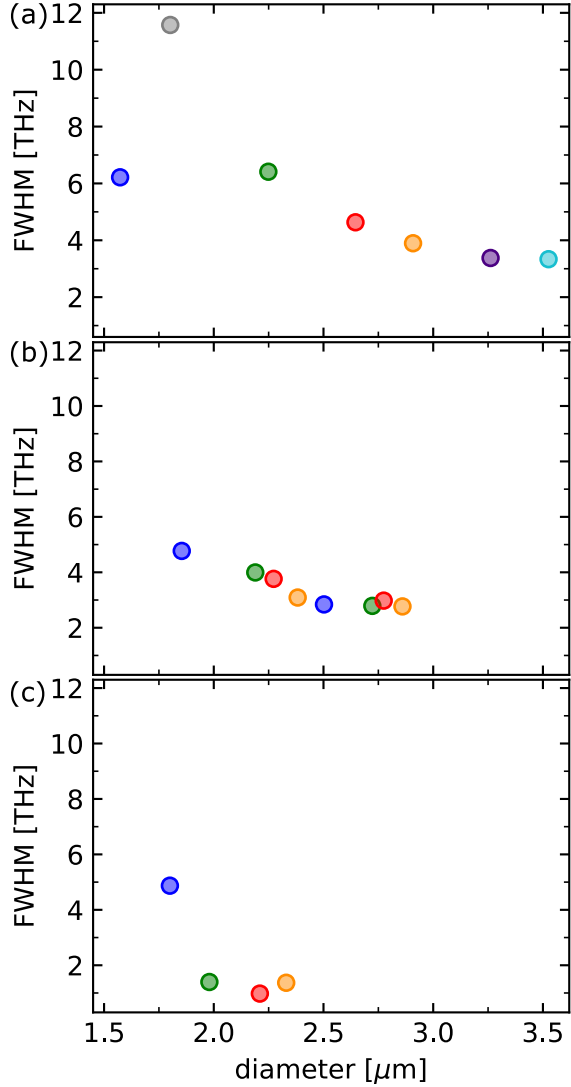

Figure 5: (a) Full-Width at Half-Maximum (FWHM) of the magnetic polariton resonances (MP1) as a function of the disc diameter. (b) FWHM of MP1 corresponding to the double-diameter configuration. (c) FWHM of MP1 corresponding to the quadruple-diameter configuration. The same color codes as in the main text are used.

compute the first-mode of the magnetic polariton (MP1) in each unit-cell as the one shown in Figure 1a of the main text. Briefly, the metallic components (Au disc and Au film) are simulated as inductors composed of the mutual inductance of parallel plates (L_m) and the contribution of drift-electrons (L_e). These components are linked by capacitances (C_m) generated between them and the dielectric layer. Additionally, a parallel plate capacitance (C_g) is introduced to approximate the gap capacitance between neighboring discs. Accordingly, the impedance of such a unit cell can be expressed as:[5]

$$Z_D = \frac{i\omega(L_m + L_e)}{1 - \omega^2 C_g(L_m + L_e)} + \frac{2}{i\omega C_m} + i\omega(L_m + L_e),$$

$$(4)$$

where

$$C_g = \frac{\epsilon_0 t_m}{\Lambda - D}, \tag{5}$$

$$C_m = \frac{c_1 \epsilon_d(\omega)\epsilon_0 D}{t_d}, \tag{6}$$

$$L_e = -\frac{D}{\omega^2 \delta(\omega)\epsilon_0}\left(\frac{\epsilon_{m,1}(\omega)}{\epsilon_{m,1}^2(\omega) + \epsilon_{m,2}^2(\omega)}\right), \tag{7}$$

$$L_m = 0.5\mu_0 D t_d. \tag{8}$$

Here, D is diameter of a disc, Λ is the periodicity of the unit cell (equal in both directions of the plane). t_d is the thickness of the dielectric layer and t_m the thickness of each metallic component. The electric permitivity of free space is $\epsilon_0 \approx 8.85 \times 10^{-12}$ Fm^{-1} and its magnetic permeability is $\mu_0 \approx 4\pi \times 10^{-7}$ Hm^{-1}. The complex dielectric function of the dielectric layer is $\epsilon_d(\omega)$. The real and imaginary parts of the di-

electric function of the metal are $\epsilon_{m,1}(\omega)$ and $\epsilon_{m,2}(\omega)$, respectively. Figures 4b and 4c show the corresponding spectra used in this work.[6,7] The spectral skin-depth of the metal is $\delta(\omega) = c/(2\omega\kappa_m(\omega))$. The speed of light in vacuum is $c \approx 2.99792458 \times 10^8 \ \mathrm{ms}^{-1}$ and the extinction coefficient of the metal is calculated as $\kappa_m(\omega) = \sqrt{0.5\sqrt{\epsilon_{m,1}^2(\omega) + \epsilon_{m,2}^2(\omega)} - 0.5\epsilon_{m,1}(\omega)}$.

The parameter c_1 is a phenomenological constant which takes into account the charge distribution on the absorber. For very long strips it is known that $0.18 \lesssim c_1 \lesssim 0.23$. In this case, we have found by comparison with COMSOL simulations that $c_1 \approx 0.15$ is a better choice for discs. This is further confirmed by comparison with experimental results on samples with single discs in a unit cell (see Figure 3b of main text) and samples with double discs in a unit cell (see Figure 4j of main text), because in both cases the charge distribution is similar. However, for a sample having four distinct discs in a unit cell, the charge distribution in the unit cell is no longer the same as in the previous cases, but is expected to increase. Accordingly, we have found that $c_1 \approx 0.19$ is a better choice for this case (see Figure 5f of main text) and smaller values make the LC model to underestimate the actual MP resonances.

The resonance condition for the first-mode of the magnetic polariton is $\Im(Z_D) = 0$, where $\Im(\cdot)$ stands for the imaginary part operator. This is an implicit equation, because it includes several parameters which are frequency dependent. Accordingly, a nonlinear numerical algorithm has been used to find the resonant frequencies.

1.3 Full-Width at Half-Maximum (FWHM)

We have computed the Full-Width at Half-Maximum (FWHM) from each absorptance spectra for single and double-diameter configurations presented in the main text (see Figures 3b and 4n of the main text, respectively). Figure 5a shows the FWHM (expressed in THz) corresponding to the MP1 resonances as a function of the disc diameter in the single diameter configuration. For large diameters, the FWHM decreases as the diameter increases and tends to a limit value for the largest diameters. This value is determined by the unit cell pitch. Nevertheless, the smallest disc shows a different trend. That is, the FWHM obtained for a disc diameter of 1.57 μm (blue) is smaller than that for a disc of diameter 1.80 μm (gray). This can be attributed to a size effect, which indicates that the FWHM increases as the Au disc diameter increases (for small disc diameters), it reaches a maximum value (as illustrated in Figure 5a) and decays to a limit value for large Au disc diameters. Therefore, additional Au discs with diameters between $1.5 - 2.0$ μm should be tested to find the one for which the FWHM reaches its maximum lifetime (minimum wavelength bandwidth). On the other hand, it is to be specified that the height of the Au disc of 1.57 μm diameter is about 58% the height of the disc of 1.80 μm diameter (see TABLE 1). Consequently, the reduction in FWHM exhibited by the blue scatter in Figure 5a is not only due to the small size of the disc diameter. Additionally, in some applications a short FHWM lifetime is preferred instead of a long one.

Figure 5b shows the FWHM of the MP1 resonances for the double-diameter configuration (see Figure 3 of main text). Scatters of the same color represent pairs of two disc diameters used in each unit cell. As in the previous case (in the large diameters range), the FWHM decreases with increasing the discs diameters. FWHM is slightly smaller with respect to the single diameter case. This could be understood as longer lifetime of the MP1 mode. The peak positions are unaffected, i.e, for a given disc diameter, the expected peak is obtained experimentally as predicted by the LC model. Thus, there is no coupling or hybridization between the two discs. Additionally, there is a clear trend on the FWHM difference between the pairs of discs, i.e., increasing the disc diameters in each pair, decreases the difference in FWHM between the discs in each pair. In particular, for the smallest pair (in blue), the FWHM difference is 1.9 THz, while for the largest pair (in orange), it is only 0.32 THz.

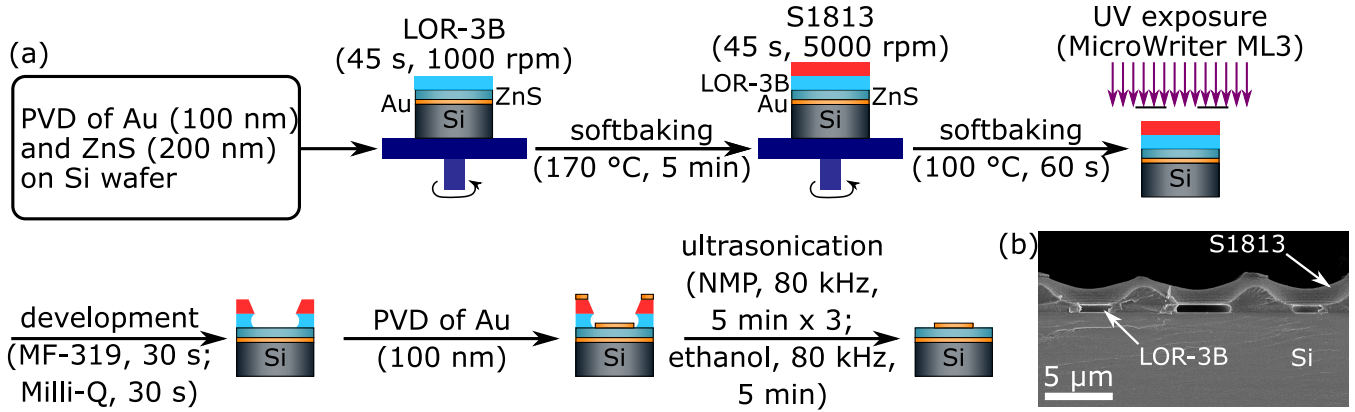For the case of the quadruple-disc sample, the

Figure 6: (a) Flow chart of the process followed for the fabrication of all samples in this work. (b) Exemplary SEM image of a cross-section after the development stage of LOR-3B and S1813 photoresists on a Si substrate.

FWHM was estimated from each gaussian curve obtained from the fit over the absorptance spectra (see Figure 5e of main text). The FWHM lifetime is similar for the three largest diameters and it increases significantly for the smallest disc diameter.

2 DETAILS ABOUT THE FABRICATION OF Au-ZnS-Au STRUCTURES

Substrates are obtained out of a 50 mm diameter Si wafer. We cleave 25 mm × 25 mm pieces out of the Si wafer. In some cases, the full wafer is used too. PVD is used for deposition of Au and ZnS layers.

After softbaking the first layer of photoresist (LOR-3B) on a substrate, it's removed from the hot plate and reserved for about 2 min to cool down at room temperature. Then, the second layer of photoresist (S1813) is spin coated and softbaked. Similarly, we wait around 2 min until the sample is in thermal equilibrium at room temperature.

The exposure of the photoresists is carried out using a MicroWriter ML3 from DMO Ltd, UK. All structures are designed in a CAD software and supplied to the DMO software as CIF files (vector graphics). The microwriter uses a provided CIF file as photomask for the UV laser during the exposure stage. Stitching errors during writing are avoided by supplying files with exposure areas of around 500 μm × 500 μm. This area is slightly smaller that the write-field size, i.e., the total area exposed once at a time. Larger areas are created using the array tool in the DMO software. We have fabricated samples in areas of 3 mm × 3 mm. The duration time of the exposure is around 5 hrs for areas of 20 mm × 20 mm. Moreover, the multi-pass exposure mode with 2 sub-divisions has been used for the fabrication of all samples. The manufacturer recommends this practice to minimize the write-field stitching by exposing each structure two times using different parts of the write-field.

For the development stage, we use three beakers: one with around 50 ml of MF-319, a second one with around 50 ml of ultrapure water and a third one for rinsing the sample with ultrapure water. Better results are obtained when stirring the substrate in vertical position. Figure 6b shows an exemplary scanning electron microscopy (SEM) image of the cross-section of the photoresists skeleton on a Si substrate after the development process. Subsequently, PVD is used for deposition of Au.

To get rid off the unwanted photoresists, the sample is submerged vertically in a glass container filled with around 60 ml of NMP for ultrasonic bath. This process is done in three steps of 5 min each to avoid heating of the sample and solvent. After, a similar process is done with ethanol absolute.
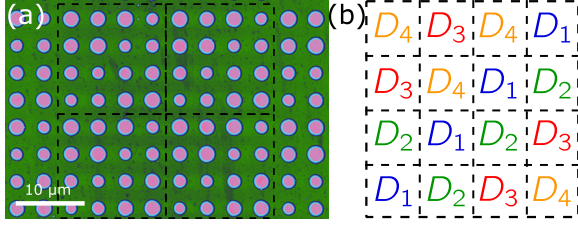
3 QUADRUPLE-DIAMETER CONFIGURATION

Figure 7: (a) Atomic force microscopy (AFM) image of the quadruple-diameter sample. A unit cell is enclosed by the dashed boundary. (b) Diagram of the code distribution of the sixteen Au discs in the unit cell. Four different discs diameters are used.

Figure 7a shows an AFM image of the quadruple-diameter configuration. This image is the same as the one presented in the main text (see Figure 5c). Additionally, the distribution of the sixteen Au discs in a unit cell, is displayed in Figure 7b. The same color code as in the corresponding SEM image (see Figure 5b of main text) is used here .

4 AFM SLOPES ANALYSIS

Figure 8a shows a diagram of a truncated cone with top radius r_1 and bottom radius r_2, the height is h. In this diagram $r_1 < r_2$, but the slope analysis is valid also for $r_2 \leq r_1$. When $r_1 = r_2$, the structure becomes a disc and for $r_2 < r_1$, the truncated cone is the upside down version of that in Figure 8a. A diagram of the slope analysis is shown in Figure 8b, the elevation angle θ measured from the substrate is equal to the descent angle θ measured from the top plane of the structure to its lateral surface. It is easily computed from the slope $(b = h/|r_1 - r_2|)$ as: $\theta = \arctan(b)$. The larger the slope, the more similar are r_1 and r_2 and $\theta \to 90°$, i.e., the structure tends to a disc shape. Additionally, the complementary angle $(\phi = 90° - \theta = \arctan(1/b))$ measures the tilt of the lateral surface with respect to the normal to the substrate and can be used to express the deviation from the disc shape: the smaller the inverse slope $1/b$, the more similar are r_1 and r_2 and $\phi \to 0°$. We find an angle $\theta \approx 90°$, indicating that our fabricated disc array is close to the ideal structure.
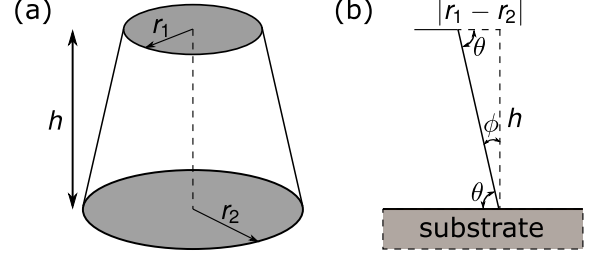
Figure 8: (a) Diagram of a truncated solid of height h, bottom diameter $2r_2$ and top diameter $2r_1$. (b) Cross section of a truncated solid on a substrate. The slope is computed as the ratio between h and $|r_1 - r_2|$. The elevation angle θ is computed from the slope.

Table 1: Measured Au discs dimensions of the studied samples.

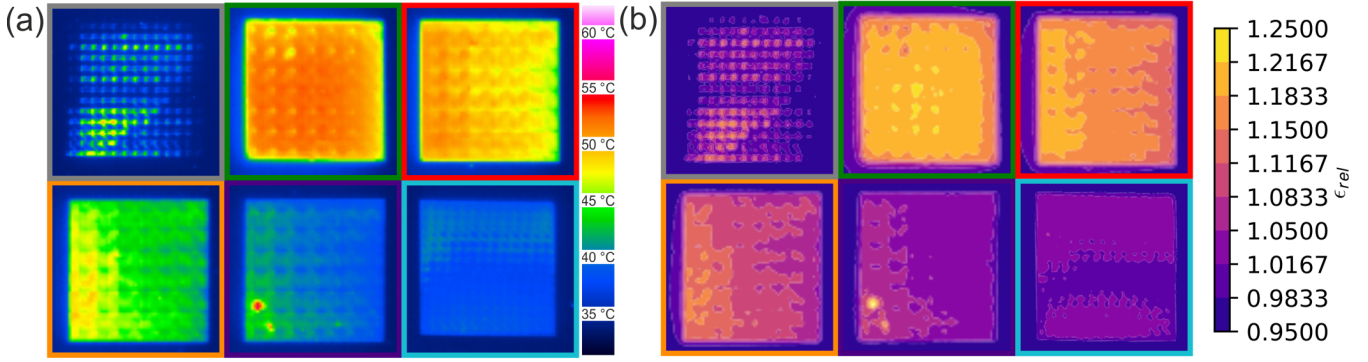| Au disc	diameter (μm)	height (nm)
SINGLE DIAMETER:		
blue	1.57	115
gray	1.80	199
green	2.25	191
red	2.65	192
dark orange	2.91	192
indigo	3.26	191
cyan	3.53	197
DOUBLE-DIAMETER:		
blue (D_1 & D_2)	1.85 & 2.50	94.4
green (D_1 & D_2)	2.19 & 2.72	94
red (D_1 & D_2)	2.27 & 2.77	92.7
dark orange (D_1 & D_2)	2.38 & 2.86	91.3
QUADRUPLE-DIAMETER:		
blue	1.80	96
green	1.98	96
red	2.21	96
dark orange	2.33	96

Figure 9: (a) Temperature maps (taken in the steady state) of the samples with Au disc diameters 1.80 μm (gray frame), 2.25 μm (green frame), 2.65 μm (red frame), 2.91 μm (dark orange frame), 3.26 μm (indigo frame) and 3.53 (cyan frame). (b) Relative emissivity ϵ_{rel} maps corresponding to the samples in (a).

5 DISCS DIMENSIONS

Table 1 presents the Au discs diameters and heights measured with SEM and AFM, respectively. For the color code of the single diameter configuration, refer to Figure 3 of the main text. For the color code used in the double-diameter configuration, see Figure 4 of the main text. For the color code used in the quadruple-diameter configuration, see Figure 5 of the main text.

6 THERMOGRAPHIC TEST

The thermal images were taken with an IR-Camera (VarioCAM®HD research 875) that is sensitive in the spectral region between 7.5 - 14 μm. For the acquisition a 30 mm objective with an close-up objective extension (0.5 x) was used. The samples were placed on a heat stage set to 100 °C. The thermal images were recorded only after that the steady-state was reached. Therefore, the relative emissivity is computed using $\epsilon_{rel} = (T_{sample}/T_{substrate})^4$. Figure 9a shows the temperature maps of the samples with Au disc diameters 1.80 μm (gray frame), 2.25 μm (green frame), 2.65 μm (red frame), 2.91 μm (dark orange frame), 3.26 μm (indigo frame) and 3.53 (cyan frame). The thermal image was taken in steady state conditions, therefore all samples are at the same temperature and the displayed differences in the IR camera are due to the different thermal emission of each sample. Accordingly, Figure 9b shows the computed relative emissivity ϵ_{rel} maps of the samples in Figure 9a with respect to the emissivity of the substrate. The samples with best performance for passive cooling will be those with higher relative emissivity, in this case, samples with Au disc diameters of 2.25 μm and 2.65 μm.
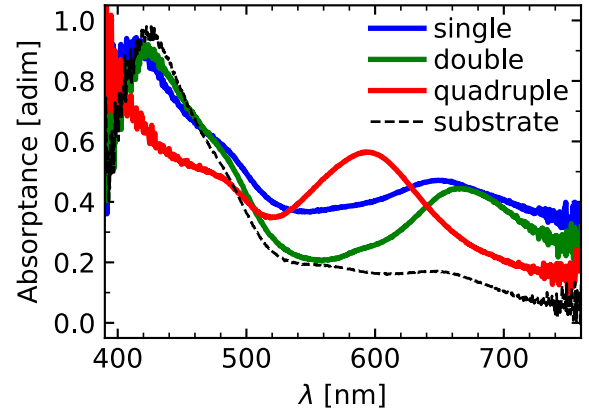

Figure 10: Exemplary absorptance spectra for single (blue line), double (green line) and quadruple (red line) configurations. Additionally, the absorptance of the bae susbstrate is plotted (dashed black line).

7 Vis-NIR SPECTRA

For the acquisition of the Vis-NIR spectra, a spectrometer (Ocean Optics USB4000) was coupled with an optical fibre (Ocean Optics, 600 μm core diameter) to the optical port of a microscope (Olympus IX71). For the sample

8

illumination a xenon lamp and a 5x objective were used. The reflectance spectra were normalized with the reflection intensity of a 100 nm silver layer. The resulting absorptance spectra is shown in Figure 10. The absorptance is larger than zero for most of the measured spectral range, which limits the applicability of the proposed structures for passive cooling applications in presence of Solar radiation.

References

(1) COMSOL®Multiphysics v. 5.4. www.comsol.com, www.comsol.com, COMSOL AB, Stockholm, Sweden (2018).

(2) Joannopoulos, J.; Johnson, S.; Winn, J.; Meade, R. *Photonic Crystals: Molding the Flow of Light - Second Edition*; Princeton University Press, 2011.

(3) Wave Optics Module User's Guide. COMSOL®Multiphysics v. 5.4, COMSOL AB, Stockholm, Sweden (2018).

(4) Tong, J.; Tobing, L. Y. M.; Luo, Y.; Zhang, D.; Zhang, D. H. Single Plasmonic Structure Enhanced Dual-Band Room Temperature Infrared Photodetection. *Sci. Rep.* **2018**, *8*, 1548(9).

(5) Feng, R.; Qiu, J.; Liu, L.; Ding, W.; Chen, L. Parallel LC Circuit Model for Multi-Band Absorption and Preliminary Design of Radiative Cooling. *Opt. Express* **2014**, *22*, A1713–24.

(6) Querry, M. *Optical Constants of Minerals and Other Materials from the Millimeter to the Ultraviolet*; Report CRDEC-CR-88009, 1987.

(7) Rakic, A. D.; Djurisic, A. B.; Elazar, J. M.; Majewski, M. L. Optical Properties of Metallic Films for Vertical-Cavity Optoelectronic Devices. *Appl. Opt.* **1998**, *37*, 5271–83.